Supporting Information

Perylene-derivatives singlet exciton fission in water solution

Chloe Magne[a], Simona Streckaite[b], Roberto A. Boto[c], Eduardo Domínguez-Ojeda[d], Marina Gromova[e], Andrea Echeverri[f], Flavio Siro Brigiano[f], Minh-Huong Ha-Thi[g], Marius Fanckevičius[b], Vidmantas Jašinskas[b], Annamaria Quaranta[a], Andrew A. Pascal[a], Matthieu Koepf[h], David Casanova[c,i], Thomas Pino[g], Bruno Robert[a], Julia Contreras-García[f], Daniel Finkelstein-Shapiro[d], Vidmantas Gulbinas[b], Manuel J. Llansola-Portoles[a*]

[a]*Université Paris-Saclay, CEA, CNRS, Institute for Integrative Biology of the Cell (I2BC), 91198Gif-sur-Yvette, France.*

[b]*Department of Molecular Compound Physics, Center for Physical Sciences and Technology, Saulėtekio Avenue 3, LT-10257 Vilnius, Lithuania*

[c]*Donostia International Physics Center (DIPC), 20018 Donostia, Euskadi, Spain.*

[d]*Insituto de Química, Universidad Nacional Autónoma de México, 04510 Mexico City, Mexico*

[e]*Université Grenoble Alpes, CNRS, CEA, IRIG, MEM, F-38054 Grenoble, France*

[f]*Sorbonne Université, CNRS, Laboratoire de Chimie Théorique, LCT, F. 75005 Paris, France*

[g]*Université Paris-Saclay, CNRS, Institut des Sciences Moléculaires d'Orsay, 91405 Orsay, France.*

[h]*Université Grenoble Alpes, CNRS, CEA, IRIG, Laboratoire de Chimie et Biologie des Métaux, F-38054 Grenoble, France*

[i]*IKERBASQUE, Basque Foundation for Science, 48009 Bilbao, Euskadi, Spain.*

*Corresponding author. manuel.llansola@i2bc.paris-saclay.fr

Table of Contents

1. Synthesis of perylene-3,4,9,10-tetracarboxylate

We synthetized a water-soluble perylene by hydrolyzing 3,4,9,10-perylenetetracarboxylic dianhydride to yield a perylene-3,4,9,10-tetracarboxylic (Hernández, Godin et al. 2013). The reagents and materials for the synthesis were purchased from Sigma Aldrich. Perylene-3,4,9,10-tetracarboxylic dianhydride (PTCDA), and KOH were used as received, with a purity of 97% and 90% respectively. To prepare the most concentrated solution of perylene-3,4,9,10-tetracarboxylate (90 mM), we added 350mg PTCDA to 10mL of 0.5M KOH solution in Milli-Q water, and sonicated for 45min at room temperature to induce the following reaction:

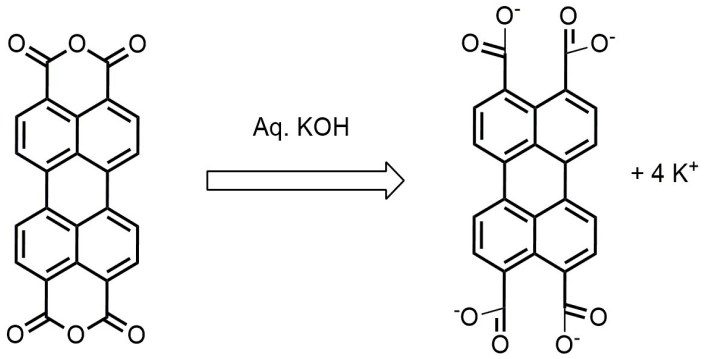

To minimize experimental error in the sample preparation, the most concentrated solution (90 mM) was used to prepare the set of diluted samples in 0.1 M KOH. Each solution was also sonicated for 10 min between dilutions and prior to each measurement.

2. Steady-State Absorption and Fluorescence

The concentrations studied for steady state absorption and fluorescence are: 0.01mM, 0.1mM, 1mM, 10mM, 30mM, 45mM, 60mM and 90mM. It must be noted that preparing solutions higher than 90 mM surpasses the solubility limit and produces a red paste. The study of the concentrated paste is out of the scope of this work. Note that to keep the absorption maxima below 1.5, and avoid saturation, we employed cuvettes/cells with different optical path lengths from 0.01 to 10 mm.

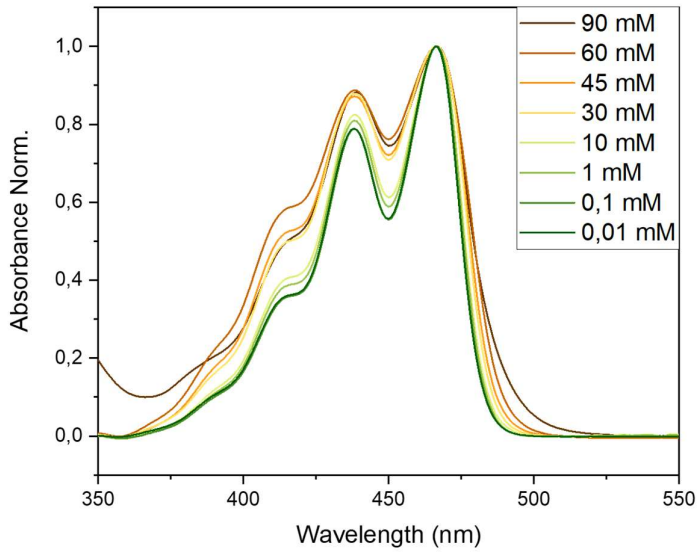

Figure S1 | Absorption spectra (specific molar absorptivity) at room temperature of perylene tetracarboxylate at 0.01, 0.1, 1, 10, 30, 45, 60, and 90 mM in water solution at pH 13.

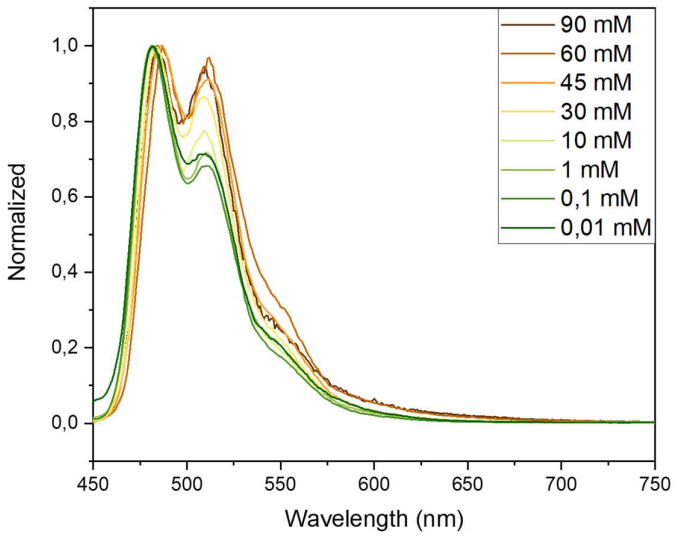

Figure S2 | Normalized fluorescence spectra at room temperature of perylene tetracarboxylate at 0.01, 0.1, 1, 10, 30, 45, 60, and 90 mM in water solution at pH 13.

3. Determination of specific molar absorptivity

Calculation of the molar extinction coefficient for the different concentrations studied (0.01, 0.1, 1, 10, 30, 45, 60 and 90 mM). Use of the Beer-Lambert formula linking Absorbance, molar extinction coefficient (M^{-1} cm^{-1}), optical path length and concentration:

$$A = \varepsilon \, l \, C \qquad \text{(eq. S1)}$$

For these measurements, different cells with different optical path lengths were used (from 0.01 to 10 mm). Details of the measurements carried out and the conditions used are shown in Table S1. The results of the ratio of the line strengths of the first two vibronic peaks in the absorption R_{abs}, are also shown in Table S1.

$$R_{Abs} = \frac{I_{A_1}}{I_{A_2}} \qquad \text{(eq. S2)}$$

Table S1. Calculated molar extinction coefficient and R_{Abs} for the different concentrations studied.

Concentrations (mM)	**90**	**60**	**45**	**30**	**10**	**1**	**0.1**	**0.01**
Cuvette Pathway (mm)	0.01	0.01	0.01	0.01	0.01	0.1	1	10
Absorbance (466nm)	0.908	1.051	1.165	0.840	0.318	0.305	0.426	0.435
Epsilon (466nm) ($M^{-1}.cm^{-1}$)	9771	17122	25062	27383	34254	32896	45905	46831

4. Time-Resolved Fluorescence (SPC)

Pico-to-nanosecond time-resolved fluorescence measurements were performed with an Edinburgh F920 (Edinburgh Instruments, UK) spectrometer. Fluorescence decay kinetics were obtained using time-correlated single photon counting (TCSPC). The excitation source was a picosecond-pulsed diode laser EPL-375 (Edinburgh Instruments, UK) emitting ~60 ps pulses (5 MHz repetition rate). The temporal resolution of this system was a few hundred ps.

To minimize self-absorption effects due to the high concentration, the samples were placed between two slices of glass (OD_{465nm} < 0.15). The decay of the fluorescence was recorded between 440-650 nm, and the intensity (I) with time (t) was fitted globally using equation S3:

$$I_{Fluorescence}\,(\lambda, t) = A_1(\lambda) * e^{-\frac{t}{\tau_1}} + A_2(\lambda) * e^{-\frac{t}{\tau_2}} \qquad \text{(eq. S3)}$$

where τ_1 and τ_2 are the lifetimes of different species, and A_1 and A_2 are their respective amplitudes for each wavelength.

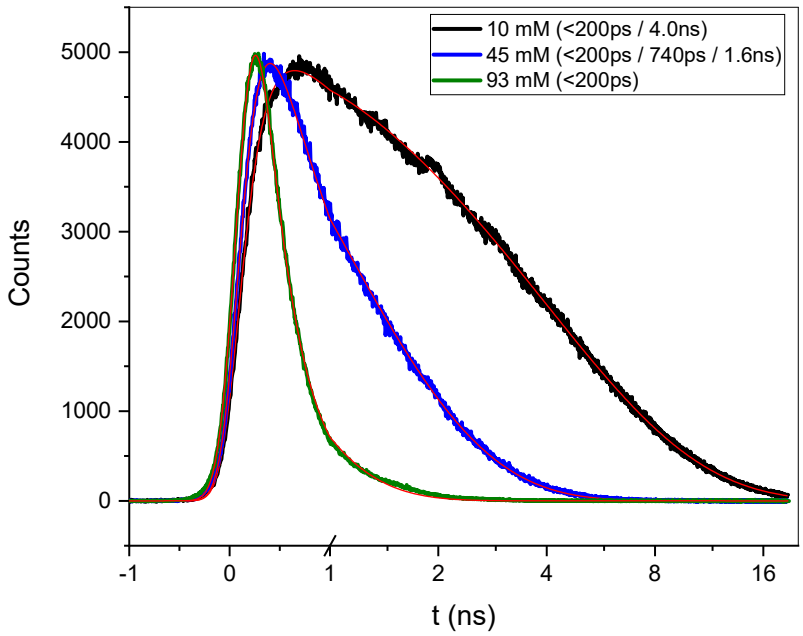

Figure S3 | Time resolved fluorescence (Single Photon Counting) collected upon 515 nm at 415 nm excitation.

5. Time-Resolved Fluorescence (streak camera)

Picosecond time-resolved fluorescence measurements were performed by using a streak camera system (Hamamatsu C5680) with synchroscan (M5675) unit coupled to a spectrometer. A femtosecond Yb:KGW oscillator (Light Conversion Ltd., Lithuania) generating 80 fs duration pulses at 1030 nm, which were frequency tripled to 343 nm (HIRO harmonics generator, Light Conversion Ltd.) at repetition rate of 76 MHz, was used for the sample excitation. Excitation energy density was attenuated using neutral density filters to about 15 nJ·cm^{-2}. The time resolution of the system was ≈8 ps. Signal acquisition time was 1-3 h for each measurement.

The decay times longer than 200 ps were obtained precisely by SPC, and then used as fixed parameters to obtain accurate values of the fastest rates. However, the 90 mM system is highly quenched and has no component longer than 200 ps. The data set needs invariably two components to yield a good fit. However, the shortest component produces good fits in the range from 15-to-25 ps as shown in Figure S4. We use this range to obtain the error in the subsequent calculation of quantum yields.

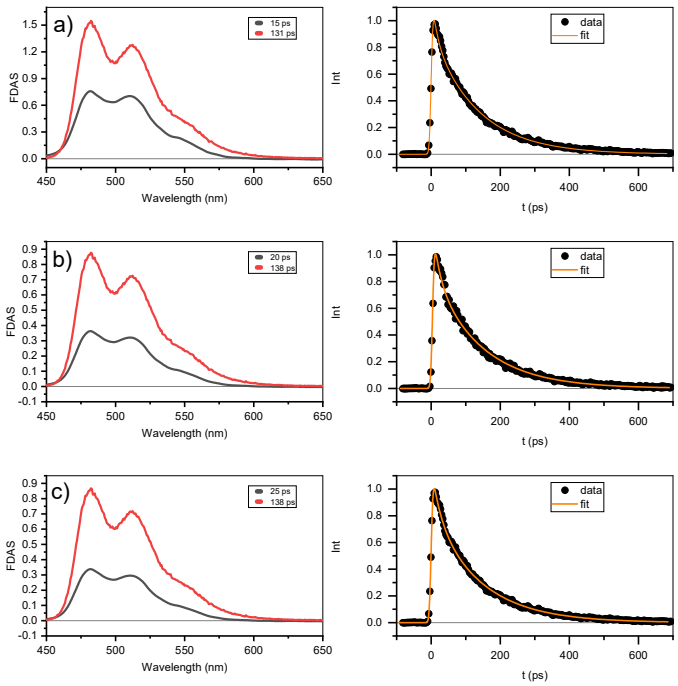

Figure S4 | Fluorescence time resolved (Streak Camera) FDAS and kinetics at 480 nm for 90 mM sample excited at 343 nm. Each panel shows several fittings to calculate the decay error.

6. Femto- to nano-second Transient Absorption Spectroscopy

6.1. Global Analysis – Sequential fit

The evolution of excited states after photoexcitation at 415 nm was fitted globally to a sequential model. Figure S5 shows the *evolution decay associated spectra* (EDAS), and selected kinetics for 10 mM, 45 mM, and 90 mM. The 10 mM can be described by a three-component model (1 ps $\rightarrow$ 200 ps $\rightarrow$ 4.0 ns) with identical EDAS. A positive feature at 740 nm due to *excited-state-absorption* (ESA) is attributed to the S_1–S_n transition, and the negative features at 515 nm correspond to *stimulated emission* (SE). The first EDAS (1 ps) shows a slight bigger ESA, this be interpreted as a relaxation of vibrationally hot-S_1. The second EDAS (200 ps) can be reasonably assigned to an excimer with strong fluorescence quenching, and the third EDAS (4.0 ns) to the monomer. It must be noted that for weak excitonic interactions, as in the present case, it has been reported that the S_1–S_n and $^1Ex_1$–^1Ex_n transitions produce indistinguishable electronic signatures (Walker, Musser et al. 2013, Margulies, Miller et al. 2016, Korovina, Chang et al. 2020). This effect is particularly evident in the work of Marguilles *et al* (Margulies, Miller et al. 2016), where the absorption spectrum of the weakly-interacting dyad shows minimal changes compared to the monomer, whereas strongly-interacting dyads exhibit distorted absorption profiles and a distinctive $^1Ex_1$–^1Ex_n transition. The spectral signatures of the S_1–S_n and $^1Ex_1$–^1Ex_n transitions create an isosbestic point at 585 nm (ΔOD = 0).

The 45 mM sample shows a dataset with a positive feature at 740 nm that disappears in conjunction with an ESA increase at 605 nm. A 5-component sequential model yields a time evolution of 1 ps $\rightarrow$ 60 ps $\rightarrow$ 740 ps $\rightarrow$ 1.8 ns. The overall evolution shows that the two initial EDAS (1 ps, 60 ps) assigned to hot-S_1, and S_1, decay to the ground state since no further evolution of species is observed. However, for the 3rd and 4th EDAS (740 ps $\rightarrow$ 1.8 ns), there is a growing ESA that peaks at 605 nm which can be interpreted as the S_1 forming an unknown specie absorbing at 605 nm. The 4th EDAS corresponds mainly to decay of this unknown species, which is not fluorescent (not detected by streak camera or SPC). Hence, the presence of significant ESA at 740 nm indicates that the sequential model cannot reproduce the observations satisfactorily.

The 90 mM sample can be fitted to a 4-component sequential model with a time evolution of 1 ps $\rightarrow$ 25 ps $\rightarrow$ 135 ps $\rightarrow$ 1.6 ns. The 1st and 2nd EDAS (1 ps, and 25 ps) show a decay of the 740 nm feature (S_1-S_n), a negative feature at 515 nm due to SE, and a small increase in the 580-610 nm region.

The 3rd EDAS (135 ps) has a strong ESA feature growing in the 580-610 nm region simultaneously with decay of the 740 nm ESA and 515 nm SE features. The 4th EDAS (1.6 ns) corresponds to the decay of the unidentified 605 nm non-fluorescent species. The fitting of the datasets to sequential models is helpful to understand the evolution of the system at different concentrations, but it cannot describe the physical processes occurring. It is clear that the S_1 state deactivates by several parallel processes.

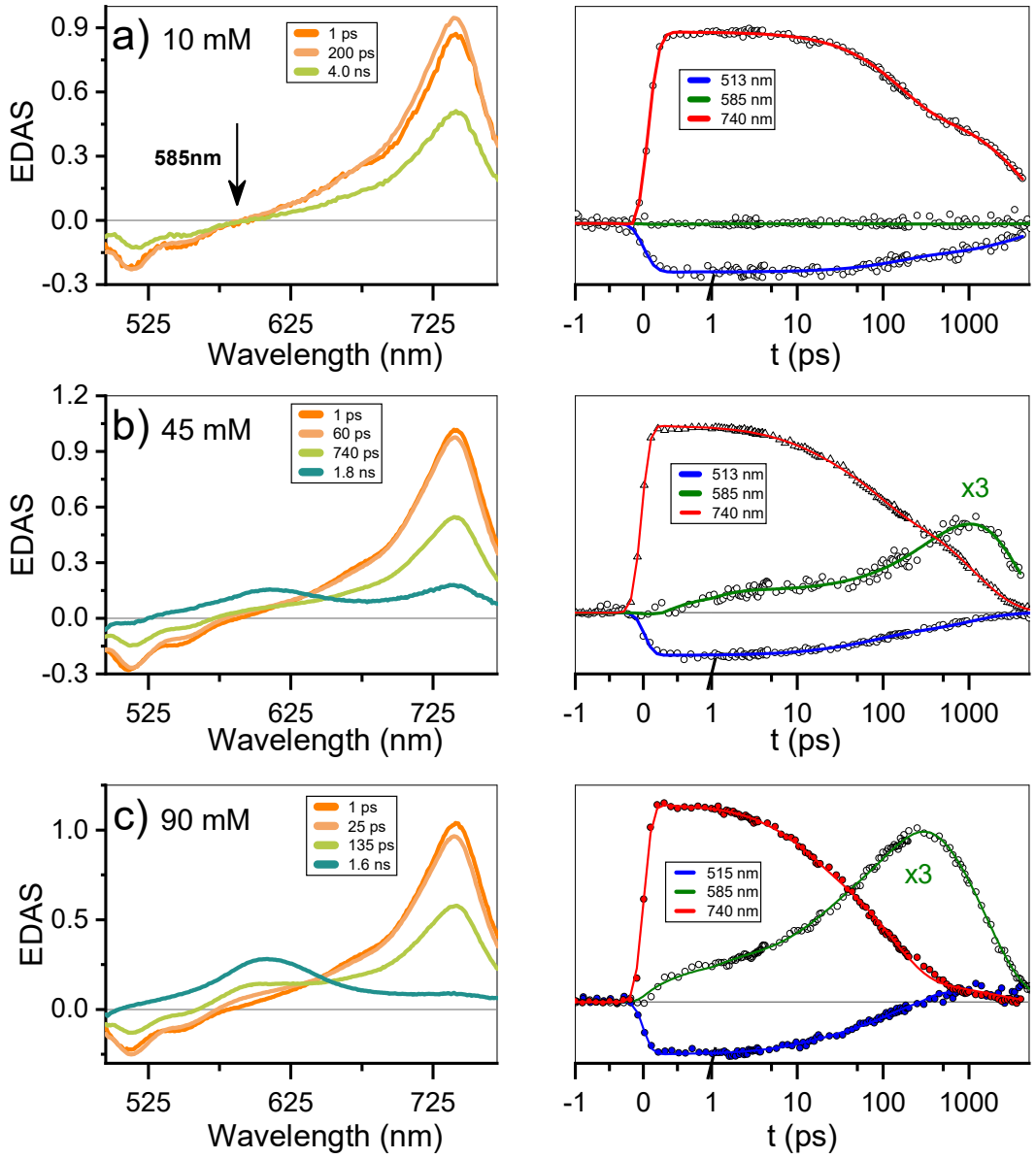

Figure S5 | Transient absorption spectra of perylene in the fs-to-ns window: EDAS, and kinetics at 515, 585, and 740 nm for **a)** 10 mM, **b)** 45 mM, **c)** 90 mM solution. Excitation wavelength:415 nm; power: 100 mW.

6.2. Global Analysis – Parallel fit

The evolution of excited states after photoexcitation at 415 nm was fitted globally to a parallel model. Figure S6 shows the *evolution decay associated spectra* (DAS), and selected kinetics for the 10 mM, 45 mM, and 90 mM samples. The data at 10 mM can be described by a three-component model (1 ps, 200 ps, 4.0 ns). It is striking that the fast component for 740 nm S_1–S_n transition is negative. It hints that there is an energy transfer between two species having the same S_1–S_n transition, in which one of them could have a slightly higher absorption. This could be interpreted as energy transfer between slightly different PTC dimers. However, this is out of the scope of this paper and the interpretation will be left for further studies of the system. Then, there are two decay components for the (positive) 740 nm ESA and (negative) 515 nm SE features, at 200 ps and 4.0 ns, respectively. The system at this concentration returns to the ground state without forming any intermediate species. It reinforces the interpretation from the sequential model, that the system contains monomers and dimers, decaying in 4 ns and 200 ps, respectively. The 45 mM sample shows a convoluted dataset with a positive feature at 740 nm that disappears along with a small ESA growth at 605 nm. The spectral signatures do not have any clear interpretation, suggesting that the parallel model is not able to capture the physical phenomena occurring with any certainty.

The 90 mM sample can be fitted to a 4-component parallel model to yield four components, decaying at 1 ps, 25 ps, 135 ps, and 1.6 ns. The 1st and 2nd DAS (1 and 25 ps) show a decay of the 740 nm feature (S_1-S_n), a negative feature at 515 nm due to SE, and a small negative feature in the 580-610 nm region peaking at 595 nm. This DAS reveals that the 580-620 nm feature is associated with the decay of the S_1–S_n transition. The 3rd DAS (135 ps) has a strong negative feature in the 580-620 nm region peaking at 610 nm, associated with decay of the 740 nm ESA and 515 nm SE. It is worth noting that the maximum of the negative feature for the 2nd and 3rd DAS are 15 nm shifted, which could indicate the formation of two different species. The 4th EDAS (1.6 ns) is the decay of the unidentified 605 nm non-fluorescent species (see above). The parallel model yields valuable insight into the different species formed, but it is still not able to capture the physical process(es) occurring. Hence, we need to develop more sophisticated schemes (see main text) to explain the observations.

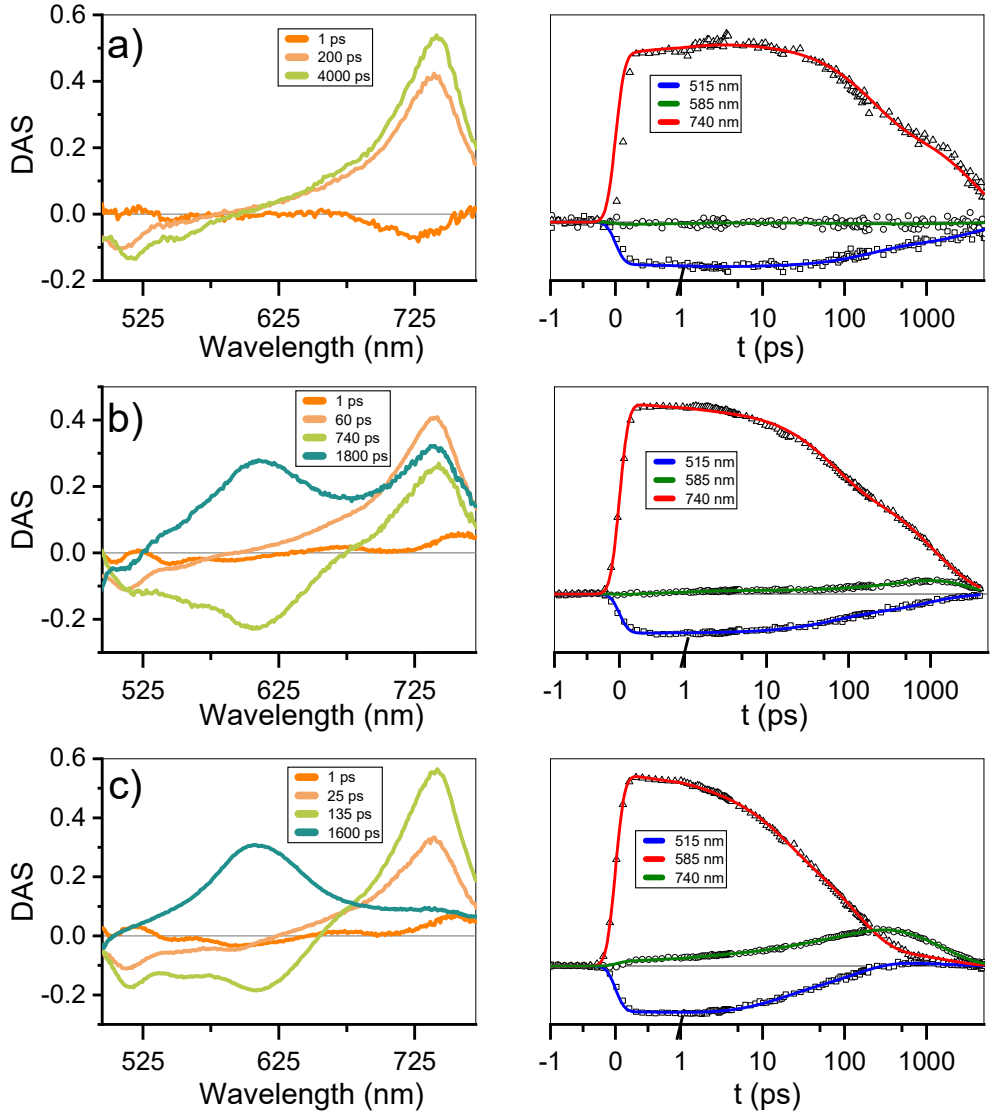

Figure S6 | Transient absorption spectra of perylene in the fs-to-ns window: DAS, and kinetics at 515, 585, and 740 nm for **a)** 10 mM, **b)** 45 mM, and **c)** 90 mM solution. Excitation wavelength at 415 nm and power 100 mW.

6.3. Power intensity

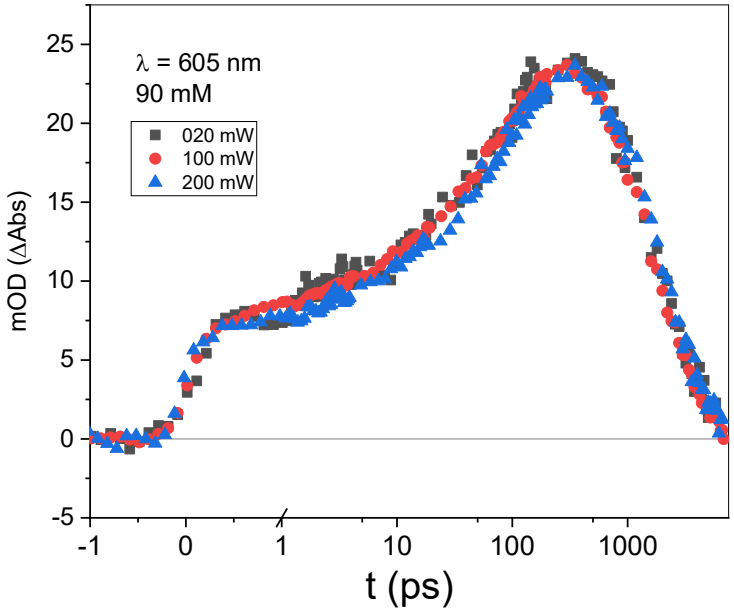

Figure S7 | Kinetic trace for 90 mM sample at 605 nm (excitation: 415 nm; power: 20, 100, and 200 mW).

7. Determination of triplet by sensitization

Sensitization measurements to unequivocally assign the signal at 600 nm to a triplet were performed using 1H-Phenalen-1-one (CAS 548-39-0) supplied by Sigma-Aldrich with 97% purity. PTC is already at its solubility limit at 90 mM, so in order to carry out the measurements in solution we had to modify the conditions of the sample as follows.

In a 70:30 water-ethanol mixture, we introduced 45 mM PTC and 45mM 1H-Phenalen-1-one. The sensitization measurements were performed by exciting into the phenalenone absorption band at 350 nm. Excited phenalenone molecules de-excite to the triplet state by intersystem crossing, with a yield close to 100%. Phenalenone triplets have a higher energy than PTC triplets, and so Triplet-Triplet energy transfer populates PTC triplet states (Knibbe, Rehm et al. 1968, Watkins 1974, Murov, Carmichael et al. 1993, Oliveros, H. Bossmann et al. 1999, Flors and Nonell 2001).

Table S2. Photophysical and energetic parameters of perylene (CAS 198-55-0) and 1H-Phenalen-1-one in different solvents (Knibbe, Rehm et al. 1968, Watkins 1974, Murov, Carmichael et al. 1993, Oliveros, H. Bossmann et al. 1999, Flors and Nonell 2001).

	Solvent	E_S (kJ/mol)	Qy fl	t_S (ns)	Qy T	E_T (kJ/mol)
Perylene	n	275	0.75	6.4	0.014	148
Perylene	p	273	0.87	6.0	0.0088	151
1H-Phenalen-1-one	Methyl-cyclohexane	299	≅ 0	-	≅ 1	185
1H-Phenalen-1-one	ethanol	299	≅ 0	-	≅ 1	186

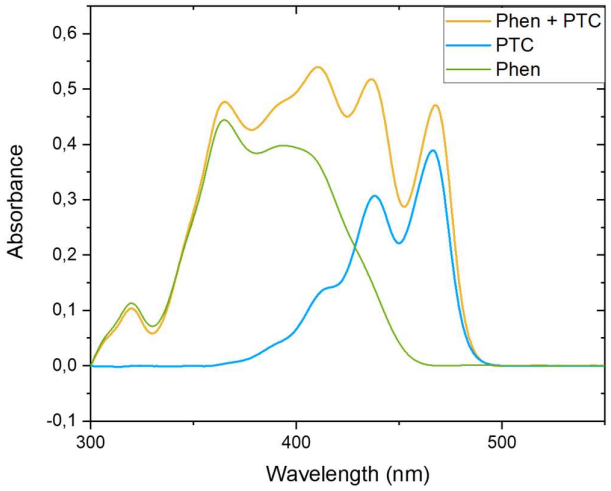

Figure S8 | Absorption Spectra of PTC, Phenaleone and the Phenalenone-PTC mixture in 70:30 water-ethanol solution (blue, green and yellow, respectively).

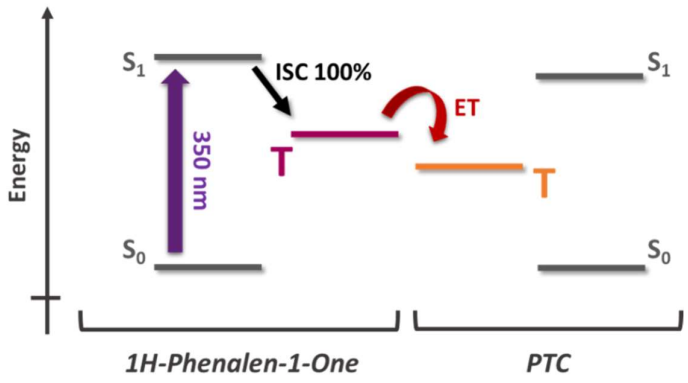

Figure S9 | Energetics scheme for T-T sensitization from 1H-Phenalen-1-one to PTC after 350 nm excitation.

8. Nuclear Magnetic Resonance

8.1. ^{1}H-NMR measurements at different concentrations

The ^{1}H-NMR spectra for all studied concentrations show a single chemical shift per distinguishable proton, an evidence of fast exchange between the different species. The individual spectra for each concentration are shown in Figs. S11-S14, and the chemical shifts are reported in Table S3.

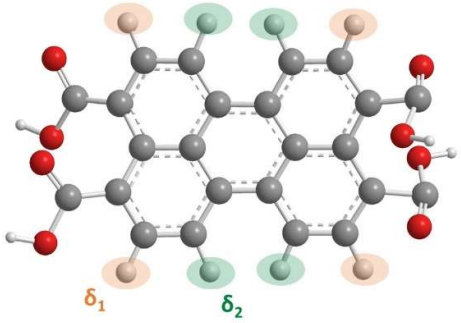

Figure S10 | Chemical shifts showing two distinct environments for the protons (δ_1 orange & δ_2 green) marked in the molecular structure.

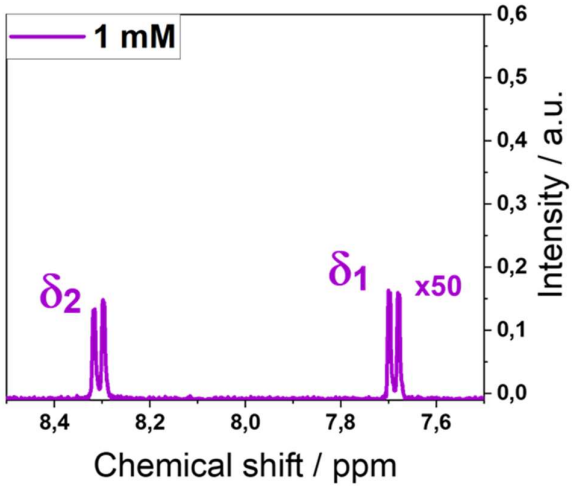

Figure S11 | 1H-NMR spectra of 1 mM PTC showing the distinct proton resonances (δ_1, δ_2).

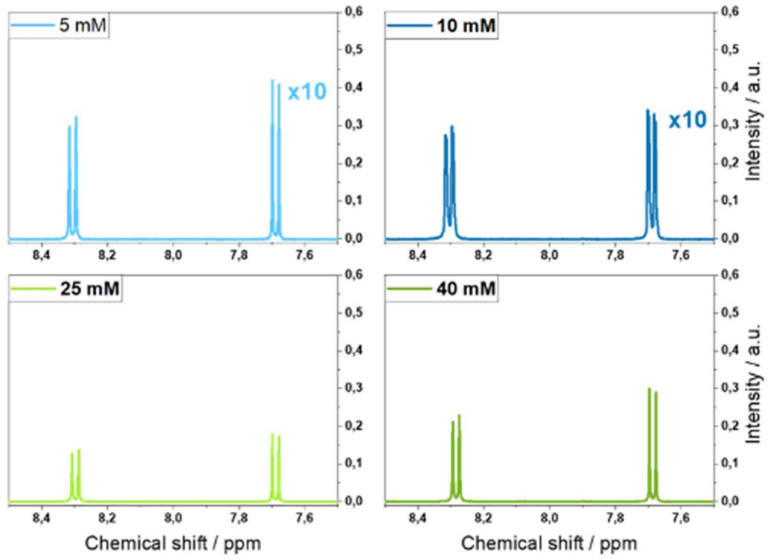

Figure S12| 1H-NMR spectra showing chemical shifts for 5, 10, 25 and 40 mM concentrations of PTC.

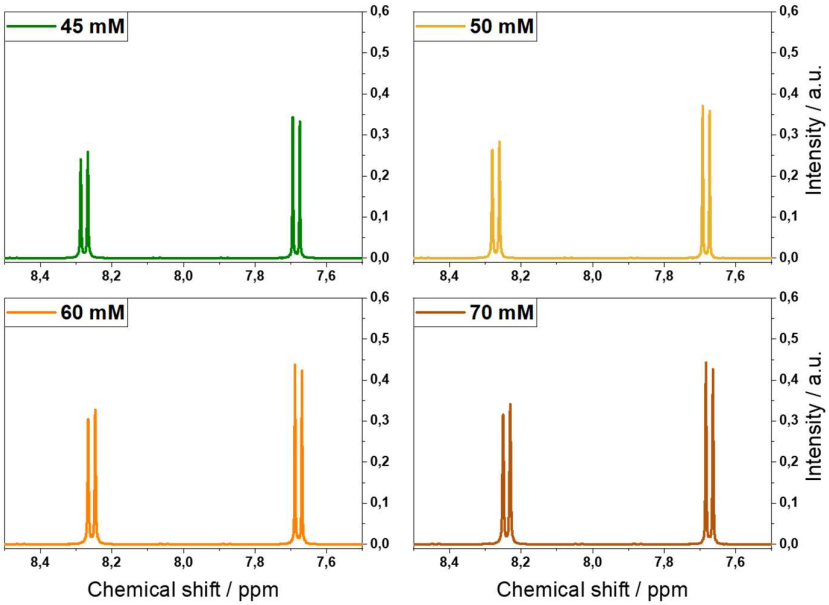

Figure S13| 1H-NMR spectra showing chemical shifts for 45, 50, 60 and 70 mM concentrations of PTC.

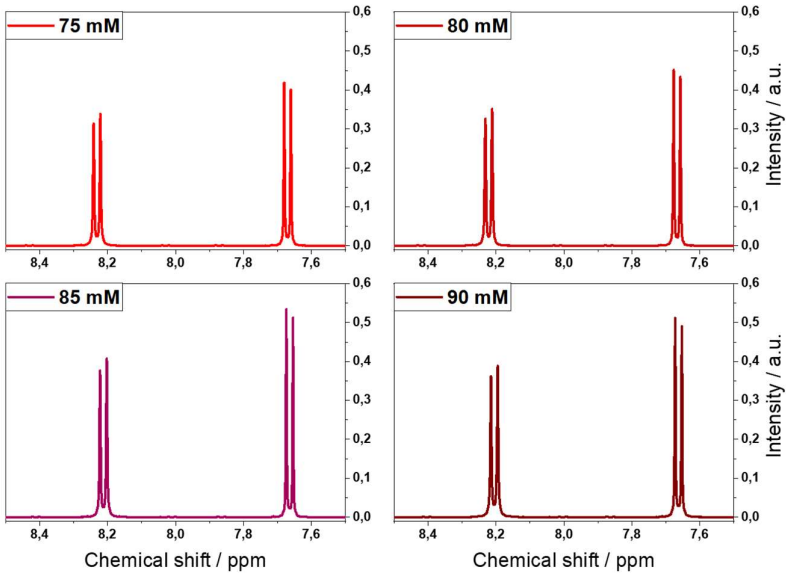

Figure S14 | 1H-NMR spectra showing chemical shift for 75, 80, 85 and 90mM concentrations of PTC.

Table S3. Chemical shifts (δ_1, δ_2) and coupling constants (J_2) for PTC at all concentrations studied.

Concentration (mM)	Delta 1 (δ_1)	Delta 2 (δ_2)	J_2 (Hz)
90	7.8073	8.3494	7.9
85	7.8088	8.3568	7.9
80	7.8116	8.3657	7.9
75	7.8148	8.3754	7.9
70	7.8175	8.384	7.9
60	7.8227	8.4002	7.9
50	7.8264	8.4138	7.9
45	7.8294	8.4217	7.9
40	7.8299	8.4272	7.9
25	7.8324	8.4404	7.9
10	7.8348	8.4495	7.9
5	7.8319	8.4485	7.9
1	7.8333	8.4516	8.0

8.2. Modelling of PTC association

We consider three possible models of aggregation, the indefinite oligomer model which has been previously observed for perylenes in organic solvents, the dimer model and the modified dimer model where each monomer first coordinates with two potassium ions before dimerizing.

Model 1: Dimers

This is one of the simplest aggregation models and is described by:

$$P + P \overset{Q_1}{\leftrightarrow} P_2 \qquad \text{(eq. S4)}$$

The predicted chemical shift within the model immediately shifts as concentration increases (see main text) and eventually saturates, which is opposite to the observed behavior of a plateau at low concentrations followed by a pronounced shift.

Model 2: formation of oligomers

The indefinite oligomer assumes an equilibrium of the form

$$P + P \overset{K}{\leftrightarrow} P_2 + P \overset{K}{\leftrightarrow} P_3 + P \overset{K}{\leftrightarrow} P_4 + P \overset{K}{\leftrightarrow} P_5 + P\ldots \qquad \text{(eq. S5)}$$

Where we assume that the equilibrium constant *K* for the species with one more molecule in the oligomer is independent of oligomer size. The oligomer model requires us to choose a cut-off number of molecules, N_{max}, for the largest oligomer. Previous studies of perylene use a cut-off maximum of N_{max}=5. To verify the dependence on the size of the largest oligomer, we carry out fits with N_{max}=5, 10 and 15 molecules shown in Figures S15, S16 and 17 and done independently from the diffusion data.

The fractional population of an oligomer of size i can be calculated as

$$f_i = \frac{{A_0}^{i-1} K^{i-1}}{(KA_0+1)^i} \qquad \text{(eq. S6)}$$

Where A_0 is the PTC concentration and *K* an association constant between the n-th and (n+1)-th oligomer, which we assume is independent of oligomer size (Wang, Han et al. 2003).

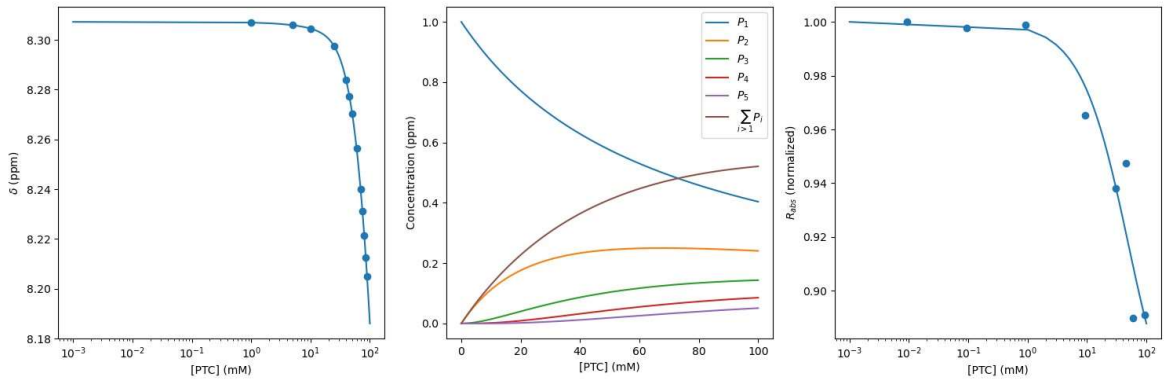

Figure S15 | Chemical shift as a function of concentration and fit using the oligomer model with cutoff Nmax=5 (left panel). Evolution of fractional oligomer populations as a function of concentration (center panel). Fit to R_{abs} using the fractional populations obtained from NMR (right panel).

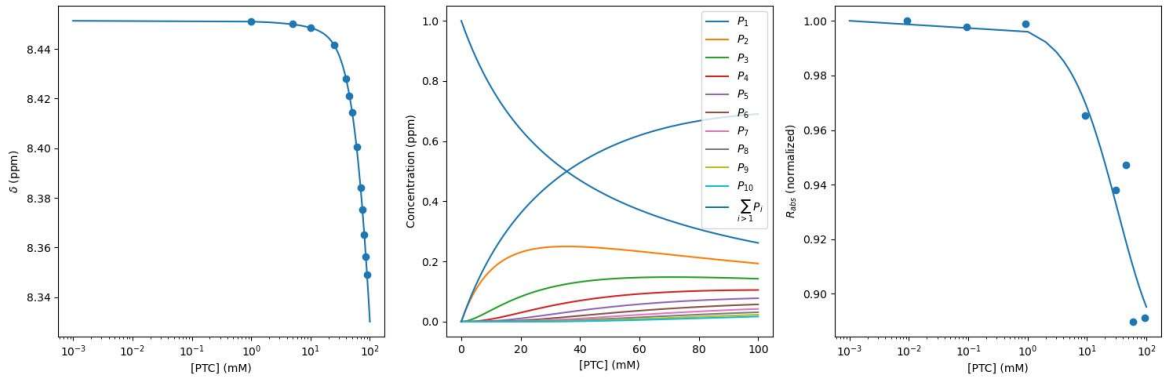

Figure S16 | Chemical shift as a function of concentration and fit using the oligomer model with cutoff Nmax=10 (left panel). Evolution of fractional oligomer populations as a function of concentration (center panel). Fit to R_{abs} using the fractional populations obtained from NMR (right panel).

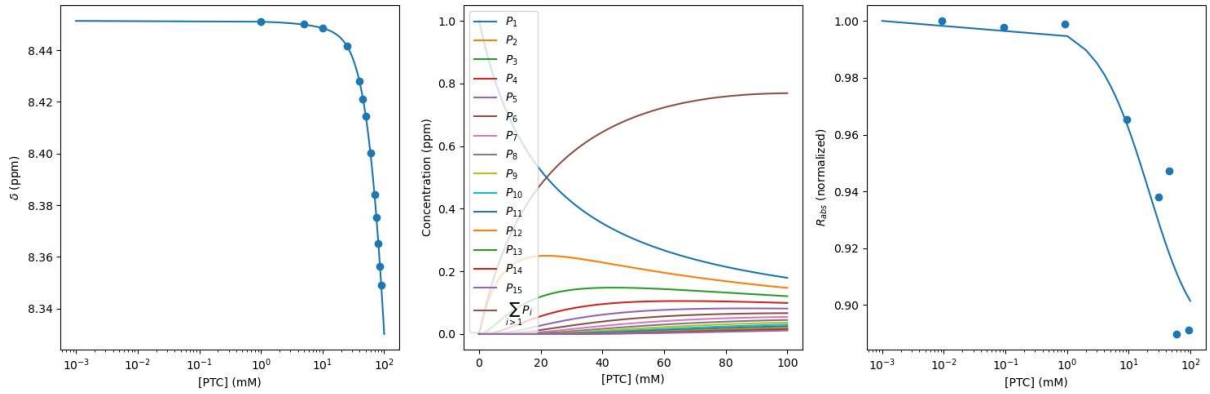

Figure S17 | Chemical shift as a function of concentration and fit using the oligomer model with cutoff Nmax=15 (left panel). Evolution of fractional oligomer populations as a function of concentration (center panel). Fit to R_{abs} using the fractional populations obtained from NMR (right panel).

Table S4. Fit parameters for oligomers with different Nmax.

5	14.76	172	40
10	28.19	122	26
15	45.67	102	18

The quality of the fit remains unsurprisingly excellent as we add more parameters. Since we cannot determine independently the chemical shift of oligomers of different sizes, the maximum size cut-off cannot be determined from the chemical shift dependence alone. We observe that the aggregation constant K increases with oligomer size to reach 45.7 M^{-1} for N_{max}=15 while monomer fractional population at 100 mM decreases with increasing N_{max} and reaches 18%. The electronic coupling constant decreases to 102 cm^{-1}. However, the fit never converges as we increase N_{max} which we would expect. Global fit with the diffusion data does not improve the fit.

Model 3: Modified dimers

We further investigate alternate models to the indefinite aggregation that could explain the chemical shift dependence. A signature of the NMR chemical shift dependence is that the upfield shift does not happen at low concentrations but is delayed until after 10 mM. The standard dimer model in dynamic equilibrium cannot explain this delayed onset of the shift. We thus consider the

formation of dimers with intermediate gating steps that we take to be the coordination of PTC with K^+ ions. The specific kinetic model is:

$$P^{|4-} + K^+ \overset{Q_1}{\leftrightarrow} PK^{|3-} \qquad \text{(eq. S7)}$$

$$PK^{|3-} + K^+ \overset{Q_2}{\leftrightarrow} PK_2{}^{|2-} \qquad \text{(eq. S8)}$$

$$PK_2{}^{|2-} + PK_2{}^{|2-} \overset{Q_3}{\leftrightarrow} (PK_2)_2{}^{|4-} \qquad \text{(eq. S9)}$$

Where Q_i=$q_{i,forward}/q_{i,backward}$ and $q_{i,forward}$ ($q_{i,backward}$) are the forward (backward) rate constants. We allow for each of the chemical species P, PK, PK_2, $(PK_2)_2$ to have distinct chemical shifts, and calculate the observed chemical shift in the fast exchange limit as weighted average

$$\delta_{observed} = f_P\delta_P + f_{PK}\delta_{PK} + f_{PK_2}\delta_{PK_2} + f_{(PK_2)_2}\delta_{(PK_2)_2} \qquad \text{(eq. S10)}$$

where f_i are the fractional populations for the *i*-th species. The fits for the model, the fractional populations as a function of PTC concentration is shown in log scale for concentration in Figure 5 of the manuscript and in lineal scale for concentration in figure S18.

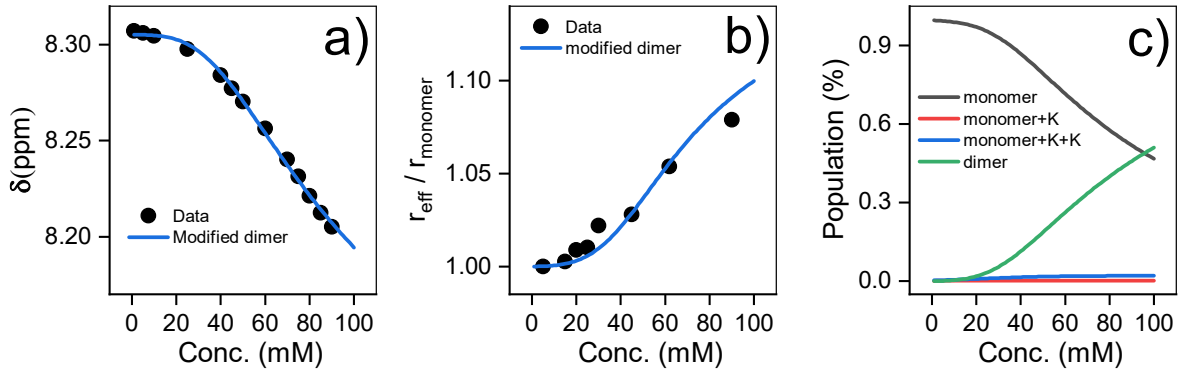

Figure S18 | a) 1H NMR chemical shift of PTC as a function of concentration, along with the fit to modified dimer model. b) Effective radius extracted from DOSY measurements fit with modified dimer model. c) Species populations for the modified dimer model.

8.3. DOSY experiments

The samples were prepared in deuterated water (D2O, 99.96%-d, Eurisotop) containing 100 µM sodium 3-(trimethylsilyl)propionate (d4-TMSP) as an internal reference; 54 mM, 39 mM, 31 mM, 22.3 mM, 18 mM, 13.3 mM, 9 mM and 4.6 mM solutions of PTC were obtained by dilution of a freshly

prepared stock solution of PTC (80 mM, in 0.5M KOH) in 0.1 M KOH. The accurate concentration of each samples were determined by quantitative 1H NMR measurements using sucrose solutions of known concentrations in deuterated water, as standards, and the ERETIC2 module to analyze the data. For the measurements, 600 µL of each solution was used.

NMR spectra were recorded on a Bruker Avance spectrometer operating at 500.18 MHz for 1H, equipped with a 5 mm z-gradient BBI probe. All measurements were performed at 298 K. Chemical shifts were reported to the TMSP signal fixed at 0.00 ppm. In pulsed field gradient 1H NMR mode, the diffusion-filtered spectra were recorded with the standard stimulated echo bipolar pulse gradient sequence (stebpgp1s). The amplitude of the trapezoidal gradient pulses (g) varying from 0.02 to 0.43 T/m. The diffusion coefficients were determined according to the Stejskal−Tanner equation:

$$\frac{I}{I_0} = exp(-(\gamma_H g\delta)^2 D(\Delta - \frac{\delta}{3} - \frac{\tau}{2}) \quad \text{(eq. 11)}$$

where I is the echo intensity at g and I_0 is the echo intensity extrapolated to zero gradient, γH is the 1H gyromagnetic ratio, D is the self-diffusion coefficient of the species considered, δ are gradient pulse duration, Δ delay during which the diffusion is observed, and τ is the time interval between the bipolar gradient pulses. The experiments were carried out with δ/2 = 1 ms, Δ = 100 ms, and τ = 0.2 ms. The recycle delay was 14 s. Bruker Topspin software package was used for processing all the spectra.

In each sample, the experimentally determined diffusion coefficient (D) was corrected by the variation of the intrinsic viscosity of the medium, estimated by measuring the diffusion coefficient of the residual TMSP.

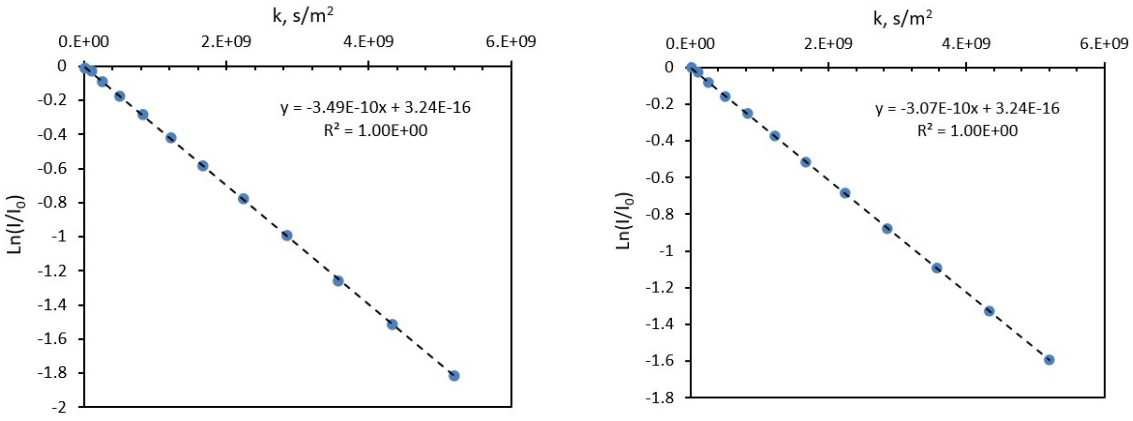

Figure S19 | Logarithmic plots of the signal attenuation for the CH resonance at ~8.4 ppm (k = (γH g δ)2(Δ − δ/3 − τ/2); for the sample containing 5 mM of PTC ($D_{measured}$ = 3.49 x 10-10 m^2s^{-1}, left), and for the sample containing 90 mM of PTC ($D_{measured}$ = 3.07 x 10-10 m^2s^{-1}, right).

Table S5. Diffusion coefficients determined experimentally for PTC ($D_{PTC\ meas}$) and TMSP ($D_{TMSP\ meas}$) for solutions of increasing concentrations of PTC in aqueous KOH solutions containing 0.1 mM TMSP, and corrected diffusion coefficient of PTC accounting for the variation of the intrinsic viscosity of the samples as determined form the evolution of D_{TMSP}.

Sample	$D_{PTC\ meas}$ (m^2s^{-1}) [a]	$D_{TMSP\ meas}$ (m^2s^{-1}) [b]	$D_{TMSP}/D_{TMSP\ 0}$	$D_{PTC\ corr}$ (m^2s^{-1})
4.6 mM	3.49(2) x 10^{-10}	5.500 x 10^{-10}	1.000	3.49(2) x 10^{-10}
9 mM	3.46(4) x 10^{-10}	5.460 x 10^{-10}	1.007	3.48(8) x 10^{-10}
13.3 mM	3.43(1) x 10^{-10}	5.390 x 10^{-10}	1.020	3.50(0) x 10^{-10}
18 mM	3.40(6) x 10^{-10}	5.380 x 10^{-10}	1.022	3.48(1) x 10^{-10}
22.3 mM	3.35(6) x 10^{-10}	5.299 x 10^{-10}	1.038	3.48(4) x 10^{-10}
31 mM	3.31(4) x 10^{-10}	5.254 x 10^{-10}	1.047	3.47(0) x 10^{-10}
39 mM	3.27(1) x 10^{-10}	5.241 x 10^{-10}	1.049	3.43(1) x 10^{-10}
54 mM	3.18(8) x 10^{-10}	5.160 x 10^{-10}	1.066	3.39(8) x 10^{-10}
80 mM	3.04(0) x 10^{-10}	4.975 x 10^{-10}	1.105	3.35(9) x 10^{-10}

[a] determined from the two aromatic signals of PTC, [b] determined from the TMSP signal fixed at 0 ppm.

Size estimation using HYDROPRO

Diffusion coefficients were estimated using HYDROPRO (Ortega, Amorós et al. 2011), from which we were able to calculate $r_{dimer}/r_{monomer}$ = 1.16. This was used to predict the effective relative radius *q* as

$$q = f_{monomer} + f_{dimer}\frac{r_{dimer}}{r_{monomer}} \qquad \text{(eq. 12)}$$

for the modified dimer model.

The structures for trimers and higher aggregates that are used in the oligomer model cannot be optimized with DFT as the binding is too weak. We make a simplifying assumption which should work as a lower bound model

$$q = f_{monomer} + f_{dimer}(1 + \Delta) + f_{trimer}(1 + 2\Delta) + \cdots \qquad \text{(eq. 13)}$$

where we have defined the relative size fractional increase $\Delta = r_{dimer}/r_{monomer} - 1$.

9. Molecular Simulations

9.1. Monomer Conformations

We determined the predominant monomer charge configuration through the following approach. Various monomers were optimized with singlet multiplicity by adjusting the total charge (-4, -3, -2, and -1; Figure S19). We then calculated absorption spectra and compared them with the 3 bands identified in the experiments (466, 457, and 414 nm). Table S6 compares the absorption wavelengths calculated for each charged species with the experimental data. This comparison reveals that the monomer with a charge of -2 and hydrogens on opposite sides of the molecule is the best match to experiment. We next observed the structural behavior of this -2 monomer in the presence of bulk water by *ab initio* molecular dynamics (AIMD). One system with monomer concentration 0.26 mol/l was generated and simulated for 30 ps in a cubic simulation box (edge length: 24.312 Å; see Fig. S21) filled with 432 water molecules (for more details on the AIMD set-up see method section in the MT). The protonation state of the monomer remained stable throughout the equilibrated AIMD trajectory (17 ps). The carboxylic and carboxylate groups are found systematically involved in strong H-bond interactions with water molecules, whereas we do not observe the formation of intramolecular carboxylate-carboxylic H-bonds during the trajectory.

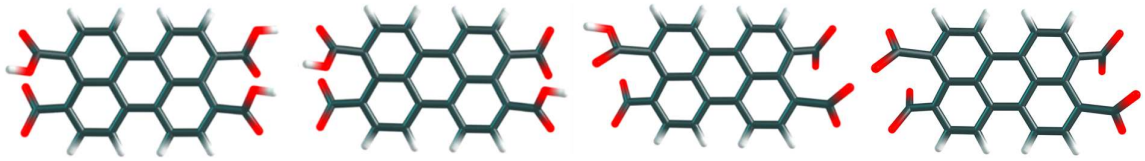

Figure S20| From left to right, geometry of the most stable tetra-substituted perylene conformer with -1, -2, -3 and -4 net charge. The geometries have been calculated with a PCM model in water at the M06/6-31g theory level.

The carboxylic O-H bonds are seen to be highly reactive in proton transfer mechanisms to water molecules and/or carboxylate groups in their proximity. This phenomenon can be appreciated in Fig. S21, where a proton transfer from a carboxylic to a carboxylate group, mediated by three water molecules, is described by the temporal evolution of the O-H bond distances of both groups. The

reaction mechanism is characterized by a decrease in the O-H1 distance (black curve in Fig. S22) and a simultaneous increase in the O-H2 distance (red curve in Fig. S22).

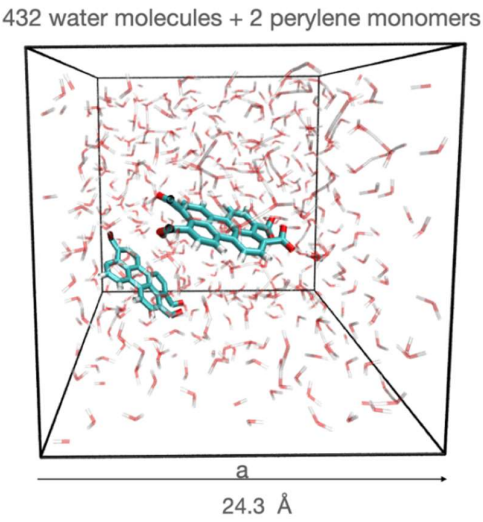

Figure S21| Boxes adopted for the simulation of the perylene monomers by AIMD. The system has a monomer concentration of 0.26 mol/l. The hydrogen atoms are depicted in white, the oxygens in red and the carbons in light blue.

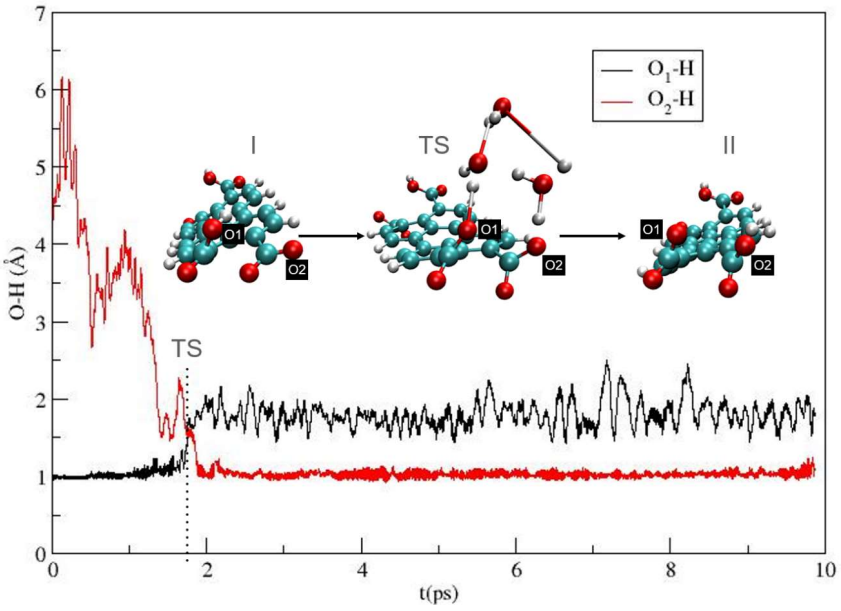

Figure S22| Temporal evolution of the carboxylic OH bonds (O1-H and O2-H) involved in the proton transfer mechanism between the carboxylic and carboxylate groups observed along the dynamics. The evolution of the O1-H and the O2-H distances in time is represented by the black and red curves, respectively; the instant of the transition is highlighted by a dashed black curve. A scheme of the reaction is shown above the traces,

going from the reactant (I) to the product (II). The carbon, hydrogen and oxygen atoms are represented in blue, red and white spheres, respectively.

Table S6| Absorption bands for different protonation states at the M06/6-31G level with PCM model in water. For twice deprotonated geometries, a) refers to those with each hydrogen located at each end of the molecule and b) for the hydrogens positioned on the same side of the molecule.

Experimental (nm)	Charge=-4	Charge=-3	Charge=-2 (a)	Charge=-2 (b)	Charge=-1
414		402	433	~444	417
457		435	~479	483-493	469
466	482	491	483	~529	486

9.2. Dimer Conformation

Structural optimization of dimers, and calculations of their vibrational frequencies and excited states, were carried out using the Gaussian 16 software (Frisch, Trucks et al. 2019). All calculations were performed with a solvent model (PCM), using a dielectric constant of 78.35 to simulate the aqueous solvent (Tomasi and Persico 1994). The configurational search for dimers was performed by placing the monomers (with a charge of -2; see above) in the center of cubic boxes of various lengths and allowing them to evolve under annealing conditions, according to the internals of the ASCEC program (Pérez and Restrepo 2008, Pérez, Florez et al. 2008, Pérez, Hadad et al. 2008). The geometric characterization is performed in terms of twist and tilt angles as defined in Figure S23.

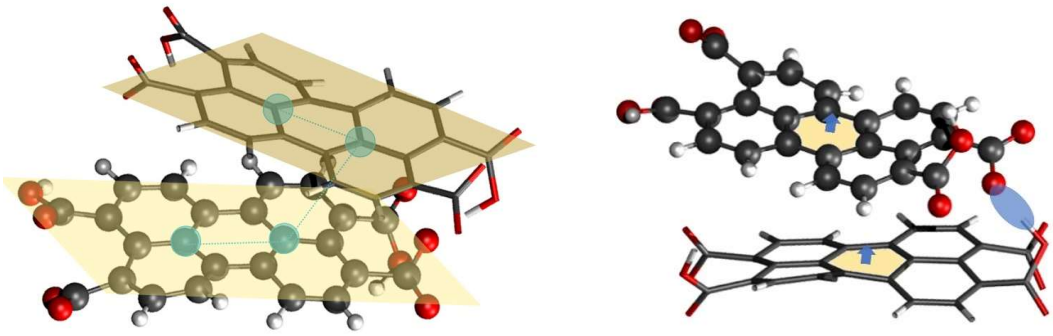

Figure S23. Schematic representation of the dimer twist and tilt angles considered. Left: The twist angle is defined as the dihedral angle formed from the three consecutive vectors connecting the four carbon atoms

which are represented as blue spheres Right: The tilt angle is defined as the angle between the two vectors perpendicular to the central C6 units of each monomer.

After the generation of candidate structures to be minima on the potential energy surface, these structures were subsequently optimized and classified as true minima by evaluating the eigenvalues of the Hessian matrix at the DFT theory level, using the functional M06 and the base 6-31g. The M06 functional was adopted because it has shown the best performance in reproducing the experimental absorption spectra of the perylene dimers (see section below for the benchmark). In Figure S27, we can see the relative energies and geometries of the 10 lowest energy dimers found with overall charge -4. The initial ten minima exhibit two distinct shapes: square types $SD1_{-4}$ -$SD6_{-4}$ and cross types $SD7_{-4}$-$SD10_{-4}$.

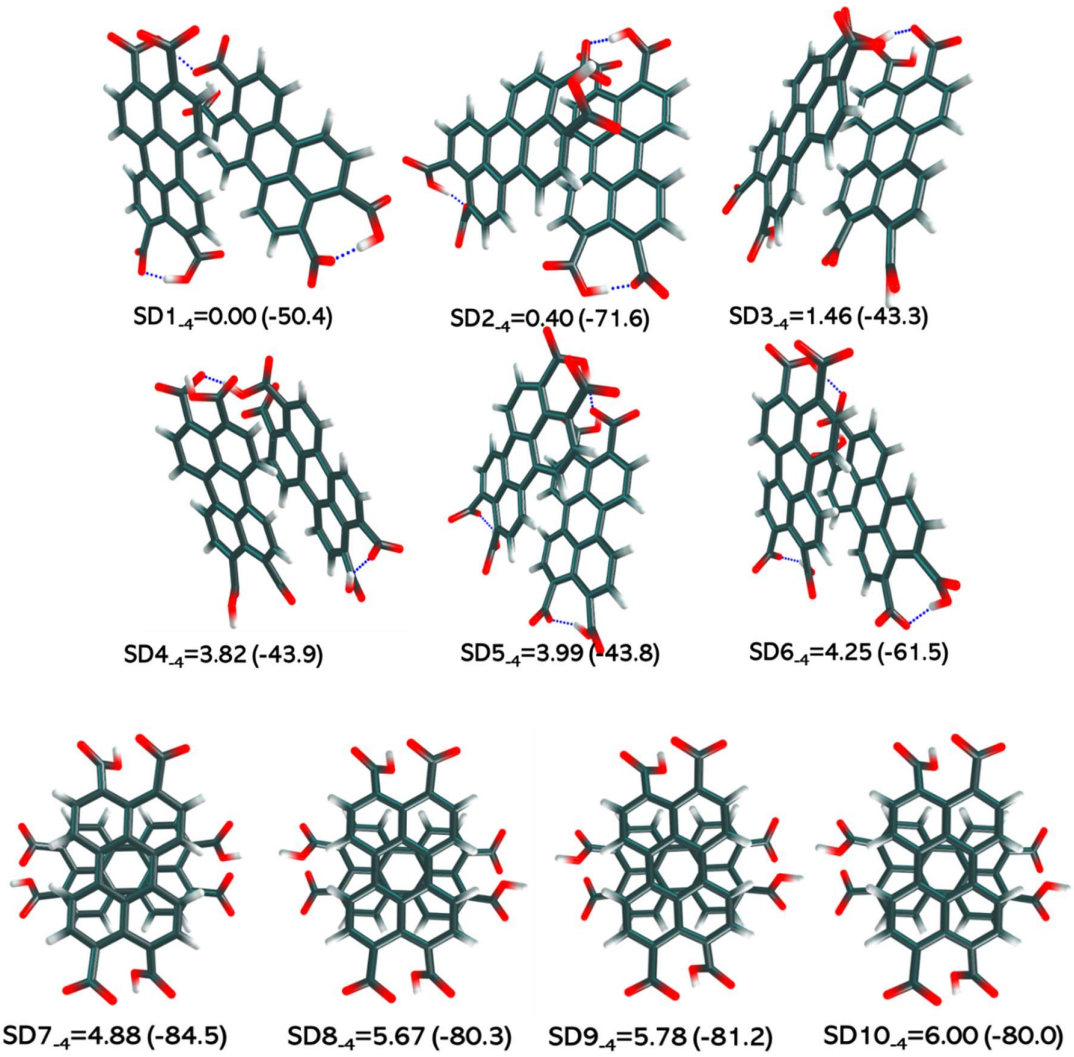

Figure S24. The first ten minima for dimers with charge -4 (relative energy indicated in kcal/mol; twist angle in parenthesis). The definition of the twist angle is shown in Figure S23. The geometries have two distinct

shapes: square types SD1-4 to SD6-4 and cross types SD7-4 to SD10-4. We can identify square-type minima by observing intermolecular hydrogen bonds between both monomers. Calculations were performed using the M06/6-31g theory level and a PCM model to simulate the aqueous solvent.

The different characteristics of the dimers are summarized in Table S7. Square-type minima are identified by the presence of intermolecular hydrogen bonds between both monomers, which explains their higher stability. These square minima can be further categorized into two subtypes: i) hydrogen bonds formed with the oxygen atoms at the edges of the carbonyl group (minima $SD2_{-4}$ and $SD6_{\_4}$), with dihedral angles ranging from -61.5 to -71.6. ii) Hydrogen bonds established with the inner oxygen atoms of the carbonyl group (minima $SD1_{-4}$, $SD3_{-4}$, $SD4_{-4}$, and $SD5_{-4}$), accompanied by dihedral angles spanning from -43.3 to -50.4. Another significant distinguishing characteristic of this initial group of compounds is the presence of intramolecular hydrogen bonding. Specifically, structures $SD1_{-4}$, $SD2_{-4}$, $SD5_{-4}$, and $SD6_{-4}$ exhibit two intramolecular hydrogen bonds, geometry $SD4_{-4}$ features only one, and geometry $SD3_{-4}$ lacks any intramolecular hydrogen bonds. In contrast, the cross-type structures (minima $SD7_{-4}$-$SD10_{-4}$), stabilized by π-stacking, primarily differ in their dihedral angles, which vary from -80.0 to -84.5.

Table S7. Relative energy in kcal/mol, adjusted with the zero-point energy, for the most energetically favorable -4 charged dimers. Calculations were performed using the M06/6-31g theory level and a PCM model to simulate the aqueous solvent

Configuration	Relative energy (kcal/mol)	Dihedral	Shape
SD1	0.00	-50.4	Square
SD2	0.40	-71.6	Square
SD3	1.46	-43.3	Square
SD4	3.82	-43.9	Square
SD5	3.99	-43.8	Square
SD6	4.25	-61.5	Square
SD7	4.88	-84.5	Cross
SD8	5.67	-80.3	Cross
SD9	5.78	-81.2	Cross
SD10	6.00	-80.0	Cross

9.3. Assessing the performance of M06 functional

In order to choose the best method to describe our system, we benchmarked the dimer experimental absorption spectrum. In Table S8, we present a comparison of the theoretical absorption spectra and associated frequencies obtained using three different functionals (CAM-B3LYP, wB97xd, and M06) against the experimental spectrum. While all three functionals reproduce the 3 bands, the oscillator strengths associated with them differ considerably. For CAM-B3LYP, the lowest-wavelength band is nearly invisible. Furthermore, the absorption wavelengths are significantly blue shifted for the CAM-B3LYP and wb97xd functionals. In contrast, M06 predicts bands at longer wavelengths that are closer to experimental values and maintain the expected relationship between them. Interestingly, we observed that the impact of the counterion on the spectrum is minimal; its main effect lies in slightly enhancing the band intensity relationship, particularly noticeable for the M06/6-31g-calculated spectrum. Hence, the M06/6-31g theory level was chosen as the most suitable for describing the system.

Table S8. Absorption bands observed in water for the most stable -4 charged dimer, along with a 4K+-like counterion, are presented across various theory levels and the 6-31g basis set with a PCM model.

Experimental (nm)	M06 (-4)	f	M06 ($4K^+$)	f	CAM-B3LYP (-4)	f	CAM-B3LYP ($4K^+$)	f	wb97xd (-4)	f	wb97xd ($4K^+$)	f
414	462	0.18	462	0.29	379	0.01	378	0.01	379	0.09	383	0.15
457	472	0.70	472	0.64	406	1.16	407	1.25	398	1.00	400	1.02
466	492	0.09	494	0.11	421	0.14	423	0.14	414	0.14	415	0.13

9.4. Discussion on S_1 and T_1 energies for the PTC monomer

We discuss here the excitation energies of the first excited singlet (S_1) and triplet (T_1) states for the PTC monomer. The energy of S_1 must be equal to or higher than twice the energy of T_1 for singlet fission to be possible. To evaluate this condition we compare the excitation energies of S_1 and T_1 obtained within time-dependent density functional theory (TD-DFT). We use the exchange-correlation functional M06 (Zhao and Truhlar 2008), which exhibits good performance for simulating the absorption bands for the PTC monomer, and the exchange-correlation functional CAM-B3LYP

(Yanai, Tew et al. 2004), which outperforms M06 in predicting singlet-triplet excitation energies (Jacquemin, Perpète et al. 2010). We use the basis set 6-31G and 6-311G(d,p) (Binkley, Pople et al. 1980), and a PCM model to simulate the effect of the solvent. We carry out all the TD-DFT calculations with the Q-CHEM program (Epifanovsky, Gilbert et al. 2021).

We show in Table S9 the simulated excitation energies for S_1 and T_1 for the molecular dianion of PTC in water. The functional M06 predicts that the SF process is slightly uphill ($E(S_1) < 2E(T1)$), but the energies obtained with the functional CAM-B3LYP indicate that SF might happen spontaneously ($E(S1) > 2E(T1)$). These results suggest that a spontaneous SF is feasible for the PTC dianion, but the balance between the energies of T_1 and S_1 is very sensitive to the quality of the DFT exchange-correlation functional. The assessment of the impact of the theory level, solvent, charge and molecular conformation on the excitation energies of PTC is beyond the scope of this work.

Table S9 |Simulated excitation energies of the S1 and T1 states for the PTC molecular dianion. Column 1: Selected density functional theory (DFT) functional and basis set. Columns 2-3: Excitation energy (in eV) of the lowest energy triplet state (T1; column 2) and the first excited singlet state (S1; column 3). Column 4: Energy difference between the energy of S1 and twice the energy of T_1.

DFT functional/basis set	$E(T_1)$ (eV)	$E(S_1)$ (eV)	$E(S_1)-2E(T_1)$(eV)
M06/6-31G	1.3321	2.6198	-0.0444
M06/6-311G(d,p)	1.3259	2.5391	-0.1127
CAM-B3LYP/6-31G	1.2533	2.9460	0.4394
CAM-B3LYP/6-311G(d,p)	1.2355	2.8274	0.3564

9.5. Evolution of excitation energies and electronic couplings with the time

In order to evaluate the excitation energies of the states involved in the SF process and the electronic (interstate) couplings that determine the SF rate, we use an excitonic model which consists of five diabatic states: two low-lying local excited states (LE), two low-lying charge-transfer states (CT), and the correlated triplet pair state ^{1}(TT) (Carreras, Uranga-Barandiaran et al. 2019). To label these diabatic states we use the subscripts 1 and 2 to refer to each of the monomers of PTC in the selected dimer configurations (see Figure S25). Monomers 1 and 2 are not equivalent, as they interact through a hydrogen bond between the carboxyl group (R-COOH) of one monomer and the carboxylate group ($R\text{-}COO^-$) of the other. In most of the selected configurations, monomer 1 donates the proton

(hydrogen bond donor) to monomer 2 (hydrogen bond acceptor) but for some configurations, the situation is reversed and monomer 1 is the hydrogen bond acceptor and monomer 2 is the hydrogen bond donor.

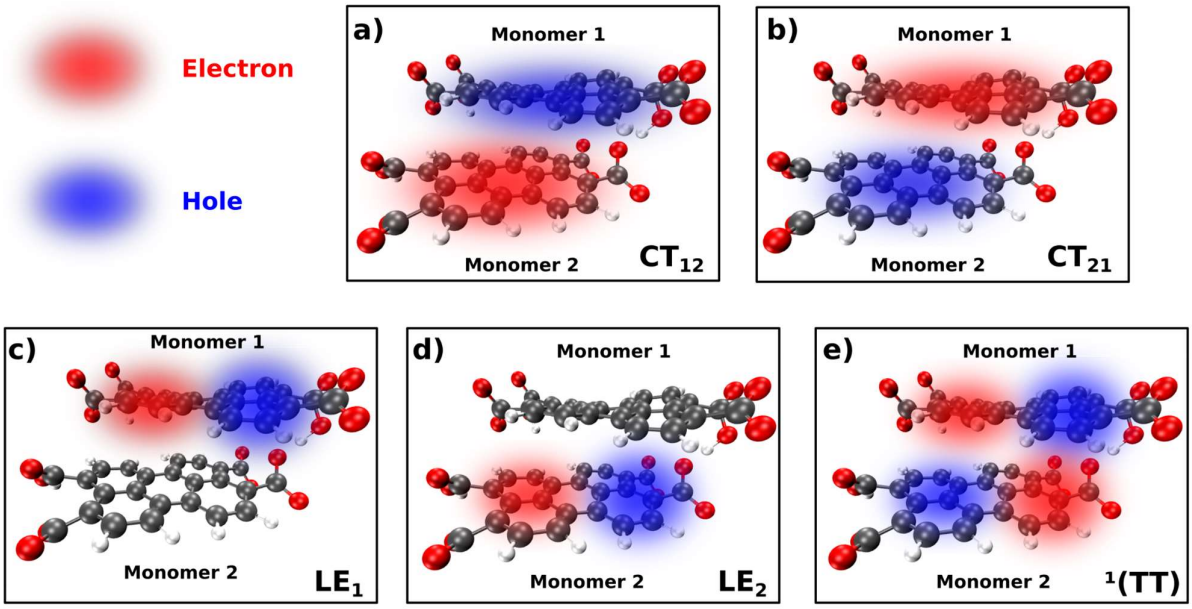

Figure S25 | Sketch of the electron distribution in the diabatic states that define the excitonic model for the PTC dimer. The red and blue areas represent regions of electron density accumulation (electron) and depletion (hole), respectively. (a) Charge-transfer state from monomer 1 to monomer 2 (CT_{12}). (b) Charge-transfer state from monomer 2 to monomer 1 (CT_{21}). (c) Local excited state localized to monomer 1 (LE_1). (d) Local excited state localized to monomer 2 (LE_2). (e) Correlated triplet-pair state ^{1}(TT). The spheres colored white, grey and red represent the atoms of hydrogen, carbon and oxygen, respectively.

We show in Tables S9 and S10 the excitation energies of the lowest energy diabatic states (Table S9) and the electronic couplings (Table S10) between the selected states computed at the RASCI(4,4)HP/6-311G(d,p)(Binkley, Pople et al. 1980, Casanova 2022) (see Experimental Section in the main text for further details on the methodology) for eighteen structures of the PCT dimer selected from the AIMD simulation. We analyze the last 17 picoseconds of the AIMD simulation and select one structure per picosecond of the simulation. We show in table S10 the electronic couplings depicted in Figure 7c-d in the manuscript.

Table S10 |Electronic couplings (see Simulation section in the main manuscript for computational details).

Interlayer distance (pm)	Twist angle (deg)	CT-med (ev)	Exciton (ev)	Direct (ev)
439.26	37.139	6.6179E-4	0.02697	0.002
481.9	30.917	0.00395	0.07174	0.00577
464.3	32.996	0.00518	0.01814	0.0028
476.1	37.48	0.00705	0.03143	0.00367
421.1	35.686	0.01015	0.02386	0.00598
465.2	30.819	0.01295	0.05339	3.0328E-4
459.4	36.375	0.01457	0.08842	0.00437
467.3	35.267	0.01635	0.01144	0.0064
459.1	39.495	0.01638	0.02218	0.00837
445.6	41.171	0.01685	0.03734	0.00705
472.5	34.088	0.02817	0.0348	0.00619
453.7	31.756	0.04138	0.02913	0.00211
445.5	41.696	0.0414	0.01213	0.0152
446.4	44.5	0.04344	0.01207	0.0097
462.8	35.734	0.04687	0.15042	0.00417
429.9	34.395	0.11556	0.04623	0.02871
454.7	37.797	0.28509	0.06768	0.00445
461.6	39.905	0.34807	0.01926	0.006
439.26	37.139	6.6179E-4	0.02697	0.002
481.9	30.917	0.00395	0.07174	0.00577
464.3	32.996	0.00518	0.01814	0.0028
476.1	37.48	0.00705	0.03143	0.00367
421.1	35.686	0.01015	0.02386	0.00598
465.2	30.819	0.01295	0.05339	3.0328E-4
459.4	36.375	0.01457	0.08842	0.00437
467.3	35.267	0.01635	0.01144	0.0064
459.1	39.495	0.01638	0.02218	0.00837
445.6	41.171	0.01685	0.03734	0.00705
472.5	34.088	0.02817	0.0348	0.00619
453.7	31.756	0.04138	0.02913	0.00211

10. Additional spectroscopic data

FTIR spectra of the starting perylene-3,4,9,10-tetracarboxylate dianhydride (PTCA) were recorded on a PerkinElmer Spectrum-100 spectrometer equipped with a Pike Ge-MIRacle ATR-module. FTIR spectra of aqueous solutions of PTCA obtained after hydrolysis were recorded on a Thermo Nicolet 6700 FT-IR spectrometer equipped with a Diamond ATR module and a MCT photovoltaic detector. All spectra were recorded at 25°C with a resolution of 4 cm^{-1}. For PTCA spectra (16 scans), air was used as background; for the spectra of the PTC solutions obtained after hydrolysis (3 x 100 scans), 0.1 M KOH solution in water was used as the background. The spectra are background corrected and provided in absorbance.

PTC stock solutions (80mM) were prepared in 0.5 M KOH in MilliQ water. The suspension was sonicated at room temperature for 50 minutes to ensure complete opening of PTCDA. It was sonicated for 10 minutes just before taking the IR spectra.

NMR spectra were recorded on a Bruker Avance spectrometer operating at 500.18 MHz for ^{1}H, or a Bruker Avance NEO spectrometer operating at 400.20 MHz for ^{1}H and 100.63 MHz for ^{13}C, equipped with 5 mm z-gradient BBI probes. All measurements were performed at 298 K. Chemical shifts were reported to the TMSP CH_3 signal fixed at 0.00 ppm. PTC solutions were prepared as described in section 8.3.

10.1. IR spectra of the perylene derivative before and after hydrolysis

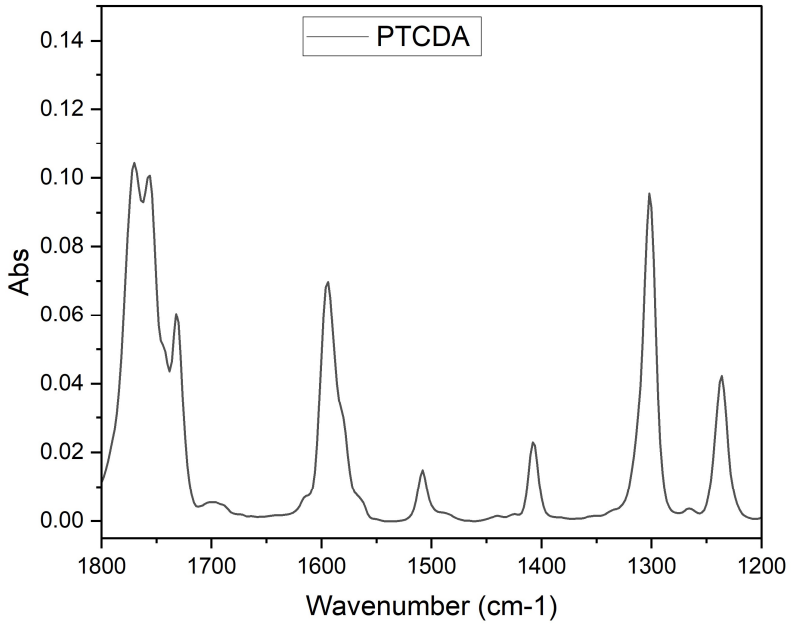

Figure S26 | FTIR spectrum (selected range) of the starting perylene-3,4,9,10-tetracarboxylate dianhydride.

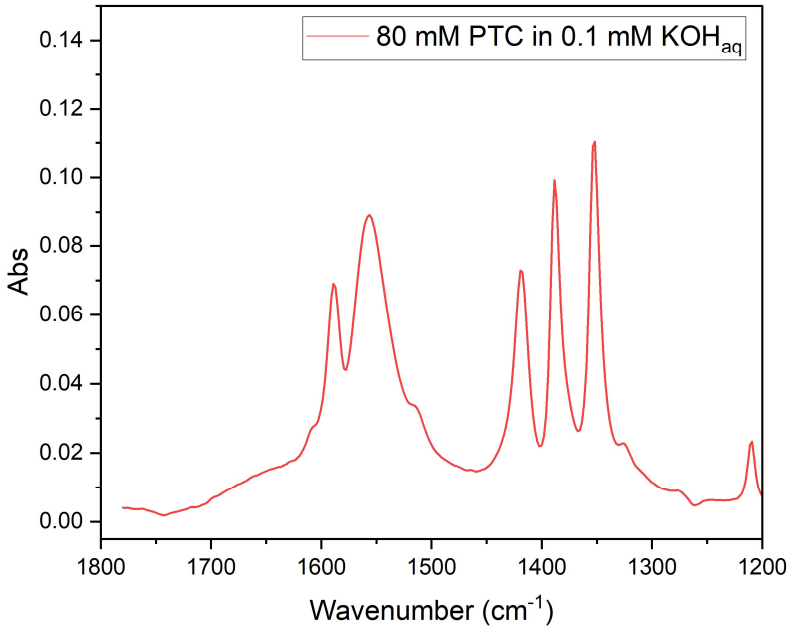

Figure S27 | FTIR spectrum (selected range) of a 80 mM solution of PTC in mQ water at 298 K.

10.2. Additional NMR spectra

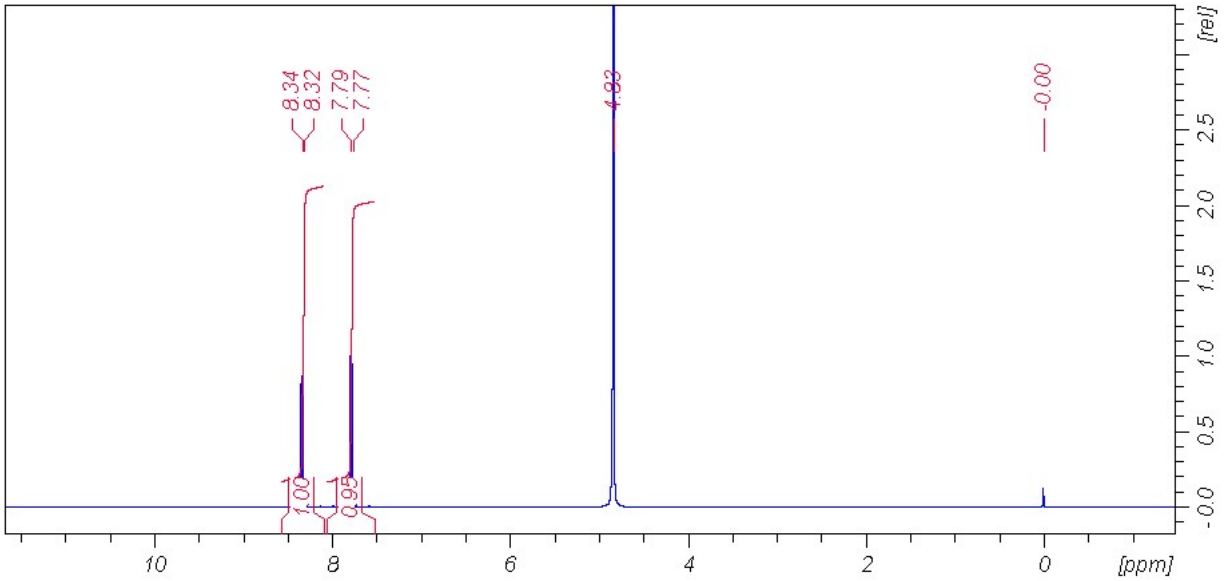

Figure S28 | ^{1}H NMR spectrum (400 MHz) of a 45 mM solution of PTC in 0.1M KOH in D_2O at 298 K.

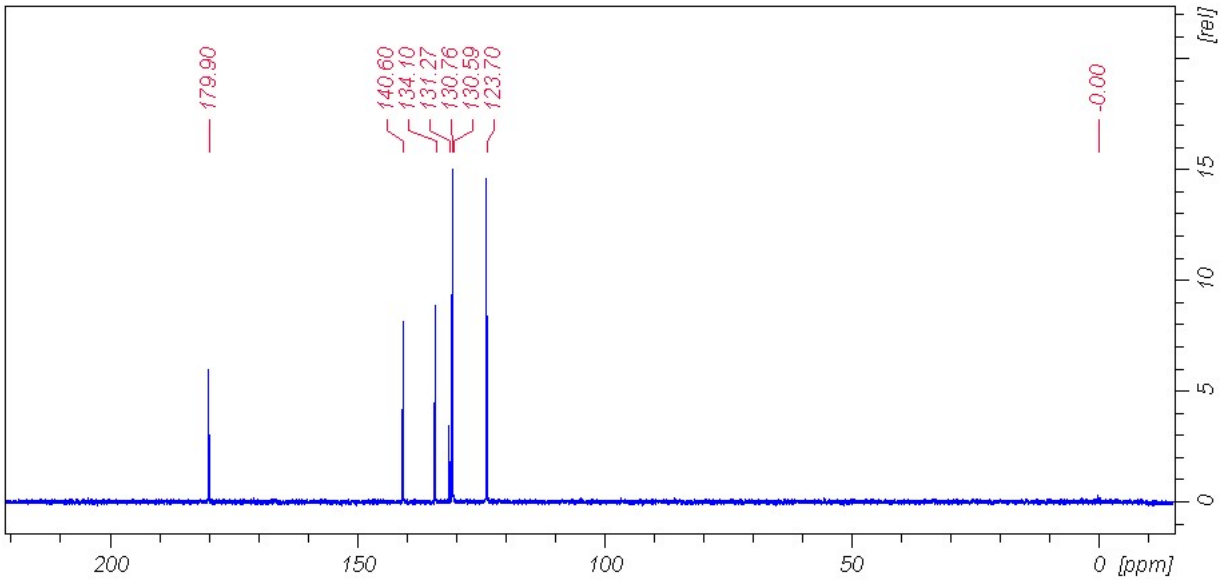

Figure S29 | ^{13}C NMR spectrum (100 MHz) of a 45 mM solution of PTC in 0.1M KOH in D_2O at 298 K.

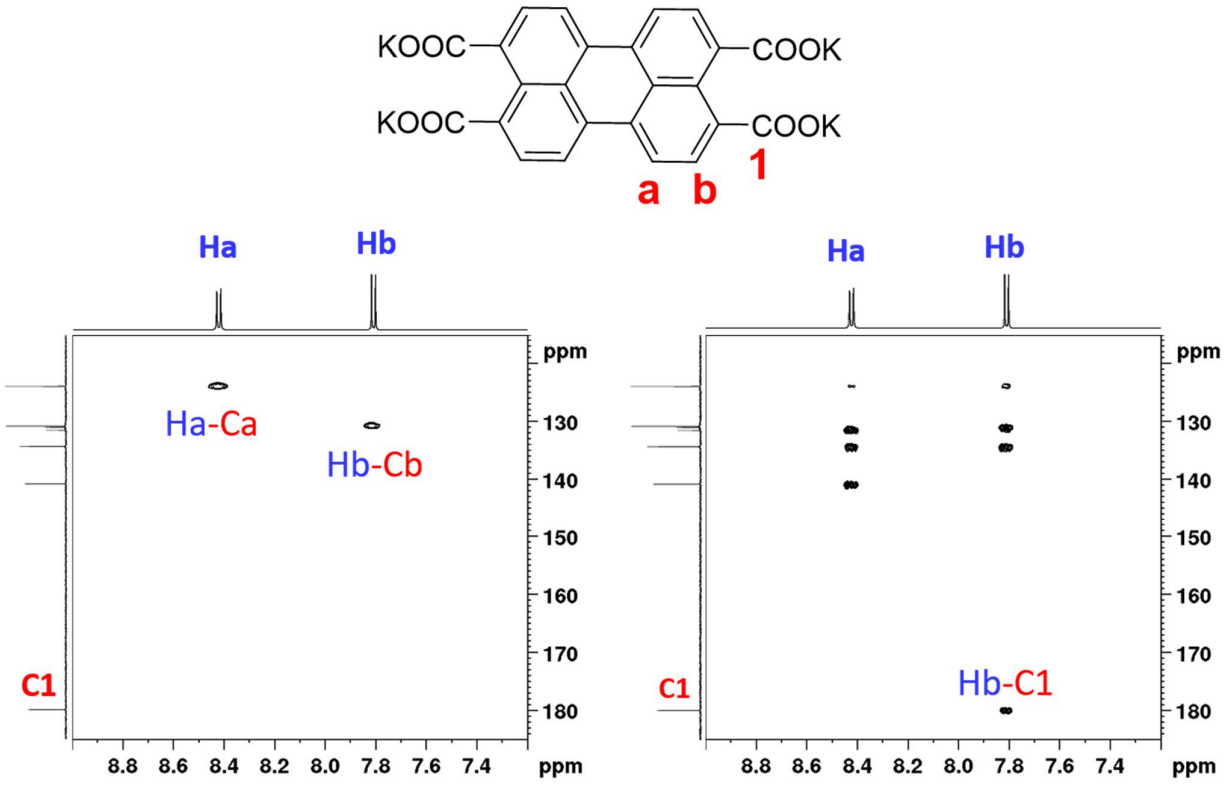

Figure S30 | ^{1}H-^{13}C HSQC (right) and ^{1}H-^{13}C HMBC (8Hz, left) NMR spectra of a 15 mM solution of PTC in 0.1M KOH in D_2O at 298 K. Partial attribution of the correlations are indicated on the spectra.

11. References

Binkley, J. S., J. A. Pople and W. J. Hehre (1980). "Self-consistent molecular orbital methods. 21. Small split-valence basis sets for first-row elements." Journal of the American Chemical Society **102**(3): 939-947.

Carreras, A., O. Uranga-Barandiaran, F. Castet, et al. (2019). "Photophysics of Molecular Aggregates from Excited State Diabatization." Journal of Chemical Theory and Computation **15**(4): 2320-2330.

Casanova, D. (2022). "Restricted active space configuration interaction methods for strong correlation: Recent developments." WIREs Computational Molecular Science **12**(1): e1561.

Epifanovsky, E., A. T. B. Gilbert, X. Feng, et al. (2021). "Software for the frontiers of quantum chemistry: An overview of developments in the Q-Chem 5 package." The Journal of Chemical Physics **155**(8).

Flors, C. and S. Nonell (2001). "On the Phosphorescence of 1H-Phenalen-1-one." Helvetica Chimica Acta **84**(9): 2533-2539.

Frisch, M. J., G. W. Trucks, H. B. Schlegel, et al. (2019). Gaussian 16 Rev. C.01. Wallingford, CT.

Hernández, L. I., R. Godin, J. J. Bergkamp, et al. (2013). "Spectral Characteristics and Photosensitization of TiO2 Nanoparticles in Reverse Micelles by Perylenes." The Journal of Physical Chemistry B **117**(16): 4568-4581.

Jacquemin, D., E. A. Perpète, I. Ciofini, et al. (2010). "Assessment of Functionals for TD-DFT Calculations of Singlet-Triplet Transitions." J Chem Theory Comput **6**(5): 1532-1537.

Knibbe, H., D. Rehm and A. Weller (1968). "Intermediates and Kinetics of Fluorescence Quenching by Electron Transfer." Berichte der Bunsengesellschaft für physikalische Chemie **72**(2): 257-263.

Korovina, N. V., C. H. Chang and J. C. Johnson (2020). "Spatial separation of triplet excitons drives endothermic singlet fission." Nature Chemistry **12**(4): 391-398.

Margulies, E. A., C. E. Miller, Y. Wu, et al. (2016). "Enabling singlet fission by controlling intramolecular charge transfer in π-stacked covalent terrylenediimide dimers." Nature Chemistry **8**(12): 1120-1125.

Murov, S. L., I. Carmichael and G. L. Hug (1993). Handbook of Photochemistry, Second Edition, CRC Press.

Oliveros, E., S. H. Bossmann, S. Nonell, et al. (1999). "Photochemistry of the singlet oxygen [O2(1Δg)] sensitizer perinaphthenone (phenalenone) in N,N'-dimethylacetamide and 1,4-dioxane." New Journal of Chemistry **23**(1): 85-93.

Ortega, A., D. Amorós and J. García de la Torre (2011). "Prediction of hydrodynamic and other solution properties of rigid proteins from atomic- and residue-level models." Biophys J **101**(4): 892-898.

Pérez, J. and A. Restrepo (2008). "ASCEC V–02: Annealing Simulado con Energía Cuántica." Property, development and implementation: Grupo de Química–Física Teórica, Instituto de Química, Universidad de Antioquia: Medellín, Colombia.

Pérez, J. F., E. Florez, C. Z. Hadad, et al. (2008). "Stochastic Search of the Quantum Conformational Space of Small Lithium and Bimetallic Lithium−Sodium Clusters." The Journal of Physical Chemistry A **112**(25): 5749-5755.

Pérez, J. F., C. Z. Hadad and A. Restrepo (2008). "Structural studies of the water tetramer." International Journal of Quantum Chemistry **108**(10): 1653-1659.

Tomasi, J. and M. Persico (1994). "Molecular Interactions in Solution: An Overview of Methods Based on Continuous Distributions of the Solvent." Chemical Reviews **94**(7): 2027-2094.

Walker, B. J., A. J. Musser, D. Beljonne, et al. (2013). "Singlet exciton fission in solution." Nature Chemistry **5**(12): 1019-1024.

Wang, W., J. J. Han, L.-Q. Wang, et al. (2003). "Dynamic π−π Stacked Molecular Assemblies Emit from Green to Red Colors." Nano Letters **3**(4): 455-458.

Watkins, A. R. (1974). "Kinetics of fluorescence quenching by inorganic anions." The Journal of Physical Chemistry **78**(25): 2555-2558.

Yanai, T., D. P. Tew and N. C. Handy (2004). "A new hybrid exchange–correlation functional using the Coulomb-attenuating method (CAM-B3LYP)." Chemical Physics Letters **393**(1): 51-57.

Zhao, Y. and D. G. Truhlar (2008). "The M06 suite of density functionals for main group thermochemistry, thermochemical kinetics, noncovalent interactions, excited states, and transition elements: two new functionals and systematic testing of four M06-class functionals and 12 other functionals." Theoretical Chemistry Accounts **120**(1): 215-241.